
Emulating malware authors for proactive protection using GANs over a distributed image visualization of dynamic file behavior

Vineeth S. Bhaskara*
Symantec Corporation
Pune, India 411 014
vineeth_bhaskara@symantec.com

Debanjan Bhattacharyya†
Symantec Corporation
Pune, India 411 014
debanjan_bhattachary@symantec.com

Abstract

Malware authors have always been at an advantage of being able to adversarially test and augment their malicious code, before deploying the payload, using anti-malware products at their disposal. The anti-malware developers and threat experts, on the other hand, do not have such a privilege of tuning anti-malware products against zero-day attacks pro-actively. This allows the malware authors to be a step ahead of the anti-malware products, fundamentally biasing the cat and mouse game played by the two parties. In this paper, we propose a way that would enable machine learning based threat prevention models to bridge that gap by being able to tune against a deep generative adversarial network (GAN), which takes up the role of a malware author and generates new types of malware. The GAN is trained over a reversible distributed RGB image representation of known malware behaviors, encoding the sequence of API call ngrams and the corresponding term frequencies. The generated images represent synthetic malware that can be decoded back to the underlying API call sequence information. The image representation is not only demonstrated as a general technique of incorporating necessary priors for exploiting convolutional neural network architectures for generative or discriminative modeling, but also as a visualization method for easy manual software or malware categorization, by having individual API ngram information distributed across the image space. In addition, we also propose using smart-definitions for detecting malwares based on perceptual hashing of these images. Such hashes are potentially more effective than cryptographic hashes that do not carry any meaningful similarity metric, and hence, do not generalize well.

1 Introduction

With the growing influence of connectivity and machine intelligence in our day-to-day life, ranging from the use of smart personal assistants like Google Assistant, to peer-to-peer connected smart cars and IoT devices, the threat landscape has become more diverse with increasing repercussions. A successful breach can range from loosing of confidential data, loss of customers, to fatalities or even death. So, it is not enough to be retroactive in protection. The existing anti-malware products mostly depend on highly specific malware-definitions based on cryptographic hashing algorithms. They use SHA256, as an example, for fingerprinting new malicious samples. However such samples reach the vendor's servers for analysis, only after some hours or days of it being first detected on a device. Most of the harm might have already been done by the time the anti-malware vendor gets the file for analysis. Instead, it is now important that the approach to stop malware must be

*Alternative Email: bhaskaravineeth@gmail.com

†b.debanjan@gmail.com

increasingly proactive, where the anti-malware product constantly creates new malware behavior “by itself”, intelligently, and discovers unknown security holes in a system even before they get exploited by a breach. Such an automated way for creation of well-defined malware programs with unique behaviors, which would be as good as the programs created by humans, is a difficult problem that not only involves modeling the logic, but also the semantics and the grammar of a programming language. We demonstrate, however, that if the malware behaviors can be approximately encoded into a representation, such as the image representation we propose, and given that, existing state-of-the-art generative models like GANs can train on them, then, one can sample representations of new malware behavior from the trained generator network, emulating a malware author.

One of the key reasons for the success of deep learning technologies, in addition to the availability of better computational power at lower costs, has been the vast scope and research in architectural engineering that constantly improved the training process and effective modeling of the priors of the problem. For example, for improving the training, the Residual Block architecture [1] with its skip-like additive connections, ensures that each subsequent layer is at least as good as the previous, thereby, addressing the gradient-vanishing problem in deeper networks. More tricks such as dropouts, non-saturating activation functions such as ReLU, first successfully demonstrated by Krizhevsky *et al.* [4], help in stabilizing the training process and improving generalization. An example of the architectural modifications to improve modeling the priors of a given problem, involves the idea of weight-sharing, for instance, within the convolution operation [2, 3] on image datasets. The weights per filter map are shared across an image to allow activation by similar localized features, and, therefore, provide translational invariance of the prediction against the semantic content of the input. Similarly, weight-sharing across time, engineered in recurrent neural networks, enables better generalization for inputs involving sequential data of arbitrary lengths. Further, data-augmentation methods [4], transformer networks [5], amongst others, are examples of architectural improvements for inputs with invariance requirements involving more general Affine transformations, including, rotation. Another important work on data-driven architectural engineering includes modeling CNNs over datasets intrinsically structured as graphs. Since a graph is defined by the vertices and the local connections, such systems require invariance of the prediction under graph isomorphism, in place of translation. For example, Duvenaud *et al.* [7] proposed CNNs over molecules with convolutions applied locally (locality defined by edges) after modeling each atom as a node in a graph of arbitrary size and shape, predicting specific chemical properties of the molecules with a great accuracy. Advances in the architectures have also involved intuition borrowed from other research fields. The recent capsule-based network architecture from Sabour *et al.* [6], for example, focuses on preserving the relative pose information of the visual entities in an image, by using units called “capsules”, which encapsulate various relative spacial information of a feature in the form of a vector, as opposed to scalar outputs from pooling neurons, drawing references from psychology and computer graphics.

In contrast, there have not been such tailored end-to-end data-driven learning models on executables, understanding their behavior, till date. This could majorly be attributed to the difficulty of engineering the architectural modifications in a neural network, that would efficiently capture the priors of the executables appropriately. Unlike the case of images where the required invariances (like translation) are common to the entire data, for executables, the invariance of the bytes per say, varies with each file based on programmer logic and the optimizations that the compiler makes. For instance, a particular chunk of bytes in a file might represent a function definition that could be invoked from some other chunk of bytes. In such a case, it makes sense to require “translational” invariance of the overall behaviour (malicious or benign) with respect to those bytes defining the function. Since different files could have such byte chunks representing the same function definition, at different offsets, and have a non-linear ordering of instructions at run-time with the programmatic constructs such as loops, jumps, etc., it becomes very hard for existing deep learning models to generalize well from such data.

Some attempts towards this direction involve a couple of recent works from nVIDIA [8] and Microsoft Research [9]. The former work implements a 1D ConvNet directly over the raw file binaries, which they refer to as MalConvNet, as a way of overcoming the memory decay in RNNs over long sequences, while the later one, models the programming constructs as graphs, building on the ideas of Duvenaud *et al.* [7]. But the efficacy of these models are far from what one expects to achieve when compared to the performance of deep learning models in other applications. Theoretically, predicting the behavior of files in arbitrary environments with static analysis of the raw binaries, is limited, due to the Halting problem that is NP-hard for an optimal solution. Though this might not be restrictive for a practical

(as opposed to optimal) end-to-end deep learning framework, it adds to the complexity of modeling over the raw bytes.

Therefore, we propose taking a dynamic analysis approach in examining the file executables, that involves monitoring the program execution on a target environment as a sequence of the low-level API calls, which determines its overall high-level behavior. In contrast to static analysis, this approach is resistant to any obfuscation of the payload by methods, such as, encryption of the corresponding raw bytes, which is generally the case with advanced malwares.

In this paper, we propose a general method for visualizing a sequence of words (events or API calls) in the form of an image that is visually distinctive, where each pixel partly encodes the overall behavior of an execution sequence, losslessly. The image representation proposed incorporates the necessary priors required for exploiting the convolutional neural network architectures in the generative (e.g. GANs) and the discriminative (e.g. deep CNN-based malware classifiers) regimes. Moreover, it is also shown to be an effective visualization technique for easy manual software or malware categorization in Section 3. Additionally, we also demonstrate how a deep Wasserstein GAN model with gradient penalty [13], referred to as WGAN-GP, can be trained over the proposed image representation of the malicious file behaviors, to assume the role of a malware author and generate new malicious behavioral-sequences; interpolating, extrapolating or even combining the behavioral features of known malwares. Such new unseen malwares can then be used to test and enhance (behavioral) signature based anti-malware solutions proactively.

An earlier work by Hu *et al.* [12] highlights an application of GANs in evading detection by generating adversarial inputs that fool existing machine learning based protection on clients. But for such an application to be practical, the malware authors must possess precise information on the features used by the classifier, which is generally kept confidential by the security vendor. It is hard for a malware author to figure out the features used, as the possible combinations (e.g. ngrams of the API calls for arbitrary n) to try out is huge. We, on the other hand, exploit GANs as malware emulators for training or testing malware classifiers against the generated malwares for proactive protection.

The rest of the paper is organized as sections in the following order:

- Mapping file behaviors to RGB images.
- Applications on Software/Malware Categorization and Smart-Definitions.
- Simple Malware Classifier trained on the behavior-mapped RGB images.
- Modeling Malware Behaviors with Generative Adversarial Networks.

Finally, we conclude by discussing on future directions, and possible improvements over the initial implementation presented[†].

2 Mapping file behaviors to RGB Images

The primary behavioral information obtained from an execution log, consists of the API (event or call) ngrams, their frequencies, and the sequence of their occurrences. For visualizing the executions, one would want to map this information to the pixel intensities of an image representation, that would allow easy manual categorization, and enable applying deep convolutional neural network-based architectures across generative and discriminative models. A trivial way of mapping such information into an image domain, might involve encoding the individual ngram words with pixel positions, and the tf-idfs of those words as their intensities. Such a image representation is *local* where a pixel corresponds to only a single feature of the behavioral trace, i.e., a single API call ngram.

We propose a *distributed* image representation, rather than a local one, where each feature corresponding to a distinct ngram partly contributes to the intensity values across all the pixels of the image.

Some considerations that motivate a distributed image representation include:

1. Being able to observe a significant difference and a certain similarity between two different executable files sharing a common sub-set of API calls but having a different overall behavior.

[†]References to the code, training parameters, dataset of files used, and the full resolution PNG figures are available at <https://github.com/bsvineethiitg/malwaregan>.

This suggests that the individual API call features must be distributed across pixels, since our visual system is more sensitive to the overall texture of the image rather than tracking specific pixels. Also, since the tf-idf (of API calls or call sequences) features are generally sparse, any local representation would be very hard to visualize, as the bright pixels would also be sparse, with most of the image being dark.

2. Encapsulating a long-range inter-dependence of the API calls across the execution, rather than just being limited by the ngrams (of API calls), such that, for example, each pixel intensity or a texture formed in the overall image representation is determined by every ngram – no matter how much they are separated in the sequence of calls.
3. Being able to apply existing deep learning techniques which work efficiently on publicly available image datasets. This requires that the priors inherently assumed of the data, by such models, remain still valid. For instance, models designed for classification tasks involving regular images assume the requirement of translational invariance of the predictions with respect to the semantic content, i.e., for example, a picture of an object of interest in a scene translated to a different location should still be classified as the same object. Under a local image representation of the file behavior, where a pixel position corresponds to a unique API call ngram, a convolutional filter map may get activated by similar pattern of pixel intensities across different parts of an image under translation. This would lead to different behaviors getting similar activations, as positions encode unique sets of the API call ngrams in a local representation. Hence, for published image-based deep learning architectures to work, an image representation needs to have uniquely identifiable patterns for different events, across the image space.

To achieve the above considerations, we exploit Fourier transform, in encoding the behavioral information into distributed image textures by mapping the frequency space with the individual API call ngram information. We elaborate the methodology of generating the image representations from the file behavior subsequently, after defining our notation for the Fourier Transform.

The Fourier Transform, $\tilde{I} = \text{DFT}\{I\}$, over a single-channel real-valued Image I of size $n \times n$ is defined by

$$\tilde{I}[i][j] = \frac{1}{n^2} \sum_{a=0}^{n-1} \sum_{b=0}^{n-1} I[a][b] e^{-\iota 2\pi \left(\frac{ia}{n} + \frac{jb}{n}\right)}, \quad (1)$$

where the indexing notation $[p][q]$ refers to the value at the p^{th} row and q^{th} column. Note that ι above represents $\sqrt{-1}$. The Fourier transform of the image, \tilde{I} , is a complex-valued $n \times n$ matrix, and therefore can be decomposed into the real and the imaginary parts, or equivalently, the amplitude and the phase parts, as illustrated below:

$$\tilde{I}[i][j] \equiv \mathcal{A}[i][j] e^{\iota \mathcal{P}[i][j]}, \quad (2)$$

where \mathcal{A} and \mathcal{P} represent real-valued $n \times n$ sized matrices corresponding to the amplitude and the phase respectively with $\mathcal{A}[i][j] \geq 0$ and $\mathcal{P}[i][j] \in [0, 2\pi)$. This operation can be implemented (per channel) using the OpenCV 2 package for Python with a few lines of code as follows:

```
amplitude, phase = cv2.cartToPolar(cv2.dft(numpy.float64(image),
                                         flags=cv2.DFT_SCALE | cv2.DFT_COMPLEX_OUTPUT),
                                   angleInDegrees=True)
```

A location in the frequency space after DFT, corresponds to a periodic texture with a unique frequency and orientation (refer to the DFT basis images, as an example, in Figure 1) in the position space, distributed across the pixels. We, therefore, encode the API call ngram words to the locations in the frequency space, with their tf-idfs determining the amplitudes in the amplitude spectrum \mathcal{A} . The phase spectrum \mathcal{P} is exploited to encode the relative ranks of the API call ngrams in the order of their first-invocation. This is repeated across the three channels (R, G, B) independently corresponding to the 4-grams, 3-grams, and 1,2-grams, respectively. Finally, a distributed image representation is obtained by applying an inverse DFT (IDFT), given the amplitude and the phase spectra, defined over a single-channel matrix \tilde{I} (with $\tilde{I}[i][j] \equiv \mathcal{A}[i][j] e^{\iota \mathcal{P}[i][j]}$) of size $n \times n$ by

$$I[a][b] = \sum_{i=0}^{n-1} \sum_{j=0}^{n-1} \tilde{I}[i][j] e^{\iota 2\pi \left(\frac{ia}{n} + \frac{jb}{n}\right)} = \sum_{i=0}^{n-1} \sum_{j=0}^{n-1} \mathcal{A}[i][j] e^{\iota 2\pi \left(\frac{ia}{n} + \frac{jb}{n}\right) + \iota \mathcal{P}[i][j]}. \quad (3)$$

Clearly, each pixel intensity in the position space depends on all the individual API call ngram features in the frequency space as evident from the above Eq. (3). This can be implemented (per channel) using OpenCV 2 as:

```
image = cv2.magnitude(cv2.idft(cv2.polarToCart(amplitude, phase,
                                             angleInDegrees=True), flags=cv2.DFT_COMPLEX_OUTPUT))
```

When visualizing the file behavior as a RGB image by this method, not only do we have the API information per channel distributed across the image, forming textures, but also, the information across the channels are intermixing, to give a rich color palette and unique patterns, to the final image for easy manual inspection and categorization as subsequently shown in Section 3.

Since the Fourier transform is reversible, one may also decode back the original API call ngrams with their first-invocation ranks and the term-frequencies, from the image representations losslessly.

We outline the algorithm for the image generation after describing the dataset below.

2.1 Dataset

Our dataset consisted of API call sequence logs over 1,984 distinct API functions, from a total of 12,006 distinct PE (.EXE) files executed through RunningWater. RunningWater is a proprietary software from Symantec, for dynamic malware analysis, that hooks itself into the running process, capturing the API call events. The samples are executed on a VM, running Windows, on a single-core. The environment is restored back after each run, to avoid any interference across the samples. The sample binaries, for our research, have been downloaded partly from the VirusTotal portal and partly from Symantec's own datastores. An example output of event sequence from RunningWater on execution of a file is as follows (ordered by the timestamp of invocation across threads)

```
...
event(1501696951,8644,3120,api_GetEnvironmentVariable(_))
event(1501696951,8644,3120,api_GetEnvironmentVariable(_))
event(1501696951,8644,3120,api_RegQueryInfoKey(21900,0,0,_,5,9,0,0,0,0,0,0))
event(1501696951,8644,3120,api_RegEnumKeyEx(21900,4,'v4.0',4,_,0,0,[3647740521,30361877]))
...
```

with the format: `event(timestamp, process_id, thread_id, api_name(args))`. The run time per sample is capped at 2 minutes with sleep times (if any) limited to 1 second. The average number of events across our dataset was about 40,000 per file execution.

In this work, we only consider the API calls as words, leaving out the arguments. One of the reasons being that, malwares, generally, tend to randomize the arguments wherever possible to evade string-based or hash-based static signatures. Therefore, from the above shown example, we only consider the following effective sequence when modeling a document representing the file behavior:

```
...
GetEnvironmentVariable
GetEnvironmentVariable
RegQueryInfoKey
RegEnumKeyEx
...
```

We reserve including arguments and loaded DLL information into the sequence, for future work. To assign labels (malicious or clean), we used Symantec's reputation service. Our final labeled dataset consisted of 1,662 clean, 2,512 malicious, and 7,832 grayware (low confidence in assigning either label) files.

2.2 Image Generation

The image representation of the API call sequence log is generated by an inverse DFT of the frequency space, where the tf-idfs of event ngrams ($n=1$ or 2, 3, and 4, mapped to the B, G, R channels, respectively) are encoded as the amplitude of a frequency component, and the relative first-occurrence order of an event is preserved in the phase information. Here, we describe the algorithm for generating $64 \times 64 \times 3$ image representation from behaviors, that may be trivially extended to the general case of $n \times n \times 3$ dimensions.

1. Each API call sequence log, out of a total 12,006 (clean+malware+grayware) file execution logs, is modeled as a document of words representing the sequence of the API call invocations per file execution.
2. Based on this corpus of documents, a vocabulary consisting of 1, 2, 3, and 4-grams is built using the scikit-learn's [14] TfidfVectorizer method as follows.

```
sklearn.feature_extraction.text.TfidfVectorizer(analyzer="word",
                                                max_df=0.98,
                                                min_df=1,
                                                ngram_range=(1, 4),
                                                norm=None,
                                                use_idf=True,
                                                smooth_idf=True,
                                                sublinear_tf=True)
```

By having $\text{max_df}=0.98$, we ignore the terms that occur in over 98% of the documents considering them similar to stop words. No normalization was used to prevent the suppression of tf-idf terms across the (1,2)-grams, 3-grams, and 4-grams, as they are treated independently while mapping to the B, G, R channels of the image, respectively. Finally, the sublinear term-frequency [15], generally defined as $1 + \log(\text{tf})$ where tf is the non-zero term-frequency, was used in order to weigh down the effect of highly repetitive API call words as it is unlikely that twenty occurrences of a term in a document truly carries twenty times the significance of a single occurrence. Moreover, this also helps, upto some extent, against good-API call spamming, a trick generally used by the malware authors to evade detection. The log nonlinearity also helps in bringing the tf-idf features across documents to a comparable numerical range without skew.

The vectorizer is fit over the corpus and transformed to generate the tf-idf vector representations for the documents in the corpus, before persisting it on disk for future use - during the prediction/evaluation phase. The vocabulary consisted of 876 unigrams, 61,052 bigrams, 365,388 trigrams, and 840,990 quadgrams after fitting it over our dataset.

3. Since an image is finite in size (in this case, $64 \times 64 \times 3$), only a limited number of the ngrams may be encoded. Therefore, we choose only the top $64 \times 64 = 4096$ ngrams per channel that correlate the most with the ground-truth labels (clean or malicious) based on a holdout set. To prevent any leakage of the label information, we randomly choose 250 samples each out of a total 1,662 clean and 2,512 malicious samples, respectively, as holdout sets for calculating the significance of the ngrams, with the below definition, that intuitively represents the ratio of the inter-class distance to the intra-class deviation.

$$\text{significance}(i) = \left| \frac{\mu_1^i - \mu_0^i}{\sigma_1^i + \sigma_0^i} \right| \quad (4)$$

Here, μ_j^i and σ_j^i respectively represent the average/mean and the standard deviation of the tf-idf values corresponding to the ngram represented by i , among the samples belonging to the class j ($j=1$ for malicious, 0 for clean).

The top 20 ngrams across channels with the highest significance measure were as shown in the Table 1.

4. Top $n \times n$ (here $64 \times 64 = 4096$) ngrams for each of the three independent channels, i.e., 61,928 1,2-grams, 365,388 3-grams, and 840,990 4-grams, are picked based on the significance measure defined in Eq. (4) calculated over the holdout set of 500 images (250 clean, and 250 malicious) as described above. These 500 images are completely removed from the dataset to prevent any information leak biasing our results. The rest of the steps are performed over the remaining 1,412 clean and 2,262 malicious files.

Table 1: Top 20 discriminating ngrams with their Inverse Document Frequencies (IDF).

ngram (n=1,2,3,4)	Significance	IDF
NtClose NtOpenKey NtQueryValueKey NtClose	0.602208	4.317899
ProcessIdToSessionId	0.593848	3.836467
RtlDeleteBoundaryDescriptor	0.571707	4.192736
NtQueryValueKey NtCreateFile	0.524891	4.634343
NtQueryValueKey NtCreateFile NtCreateSection	0.524891	4.634343
NtQueryValueKey NtCreateFile NtCreateSection NtMapViewOfSection	0.524891	4.634343
VirtualAlloc VirtualAlloc VirtualAlloc VirtualProtect	0.513892	2.501540
GetStartupInfo	0.508476	4.421983
NtClose NtQueryValueKey	0.508327	4.283998
NtOpenProcessToken NtQueryInformationToken NtClose NtOpenKey	0.506242	4.643852
NtQueryInformationToken NtClose NtOpenKey NtQueryValueKey	0.500000	4.686135
RtlDeleteBoundaryDescriptor RtlDeleteBoundaryDescriptor	0.497304	4.343512
NtOpenThreadToken	0.491294	4.477043
RtlGetNtProductType RtlDeleteBoundaryDescriptor	0.478606	4.682818
RtlDeleteBoundaryDescriptor RegOpenKeyEx	0.476774	4.669660
QueryPerformanceCounter GetStartupInfo	0.474858	4.603285
GetSystemTimeAsFileTime QueryPerformanceCounter GetStartupInfo	0.474858	4.612502
NtQueryValueKey	0.472702	1.707998
Process32Next	0.469005	3.009256
LoadLibrary ZwQuerySystemInformation	0.466916	2.442038

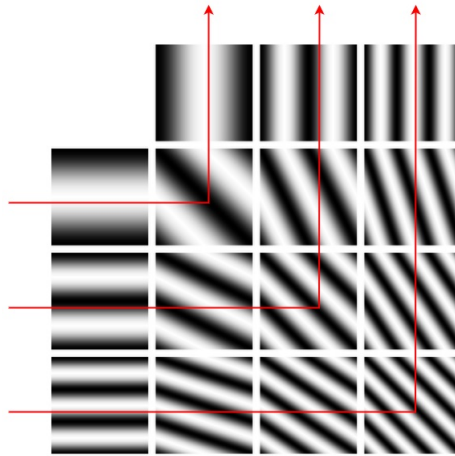


Figure 1: DFT basis images in the position space corresponding to an amplitude for a single frequency out of $4 \times 4 = 16$ possible frequencies with varying orientation where the top-left pixel represents the DC component that determines the overall brightness of the image in the position space. The arrows represent the order of assigning the ngrams based on their significance starting from the bottom-most arrow.

Table 2: Top 15 1,2-grams assigned to the positions in the frequency space of the Blue channel of a 4×4 Image. The height h (along the vertical axis) and the width w (along the horizontal axis) coordinates are measured from the top-left position labeled by $(0, 0)$.

ngram (n=1,2)	Significance	Position assigned (h, w)
ProcessIdToSessionId	0.593848	(3, 0)
RtlDeleteBoundaryDescriptor	0.571707	(3, 1)
NtQueryValueKey NtCreateFile	0.524891	(3, 2)
GetStartupInfo	0.508476	(3, 3)
NtClose NtQueryValueKey	0.508327	(2, 3)
RtlDeleteBoundaryDescriptor RtlDeleteBoundaryDescriptor	0.497304	(1, 3)
NtOpenThreadToken	0.491294	(0, 3)
RtlGetNtProductType RtlDeleteBoundaryDescriptor	0.478606	(2, 0)
RtlDeleteBoundaryDescriptor RegOpenKeyEx	0.476774	(2, 1)
QueryPerformanceCounter GetStartupInfo	0.474858	(2, 2)
NtQueryValueKey	0.472702	(1, 2)
Process32Next	0.469005	(0, 2)
LoadLibrary ZwQuerySystemInformation	0.466916	(1, 0)
CreateToolhelp32Snapshot	0.461527	(1, 1)
NtOpenKey NtQueryValueKey	0.451770	(0, 1)
DC Component (initialized with a positive value) that gets scaled on normalizing the contrast	–	(0, 0)

5. Across each channel, the higher significant ngrams are mapped to positions of higher frequency as occupied when transforming an image into frequency-space by DFT. This allows one to model better discriminating features with sharper distinctive edges into the position-space. This methodology is chosen such that the image representation is visually differentiable, for manually categorizing files. The lesser discriminative features are assigned to the lower frequency positions in the Fourier-space of the image, which, effectively, get modeled as smoother patterns in the position-space image representation. An example of the DFT basis images for the case of 4×4 dimensions are shown in Figure 1, along with a demonstration of the ngram to coordinate mapping (in the frequency-space) in Table 2 for the Blue channel ($n=1$ or 2). This is repeated similarly for the Red and Green channels, corresponding to the 4-grams and 3-grams, respectively. The top left-most pixel in the frequency space corresponds to the DC component, determining the overall brightness of the image, that gets scaled appropriately on normalizing the contrast per channel (described subsequently).
6. For each of the ngrams mapped to a position in the frequency space per channel, the corresponding tf-idf coefficients are encoded as the amplitudes in the polar representation of the DFT. We denote this by the matrix \mathcal{A}_i^j , given an executable i , across the channels denoted by $j \in \{R, G, B\}$.
7. To determine the phase component of the call ngrams mapped to the positions in the frequency space, the relative first-invocation ranks of the ngrams (i.e., in the sequence of the ngrams ordered by their first-invocation in the API call log) per channel are computed for a given executable. That is, considering the R channel, for instance, the relative ranks of first-invocation are computed among the 4-grams that occurred in the executable. The ranks assigned per channel are then rescaled to $(0, 360]$, dividing the range into equal intervals, to encode the phase corresponding to the ngram positions in the frequency space. We denote this by the matrix \mathcal{P}_i^j for a given executable i across the channels denoted by $j \in \{R, G, B\}$. Therefore, the sequence information is not only captured with the tf-idfs of the ngrams ($n>1$), but also into the phase of the image, by encoding the relative first-occurrence ranks among the ngrams per channel.

For the case of the Blue channel consisting of both 1 and 2-grams, the ngram ranks assigned among each set are merged in the same order, giving a higher precedence to the 1-grams over the 2-grams in the case of a tie. As an example, consider the sequence Q, Q, B, P. The ranks for the 1-grams would be 1, 2, 3 corresponding to Q, B, P; while

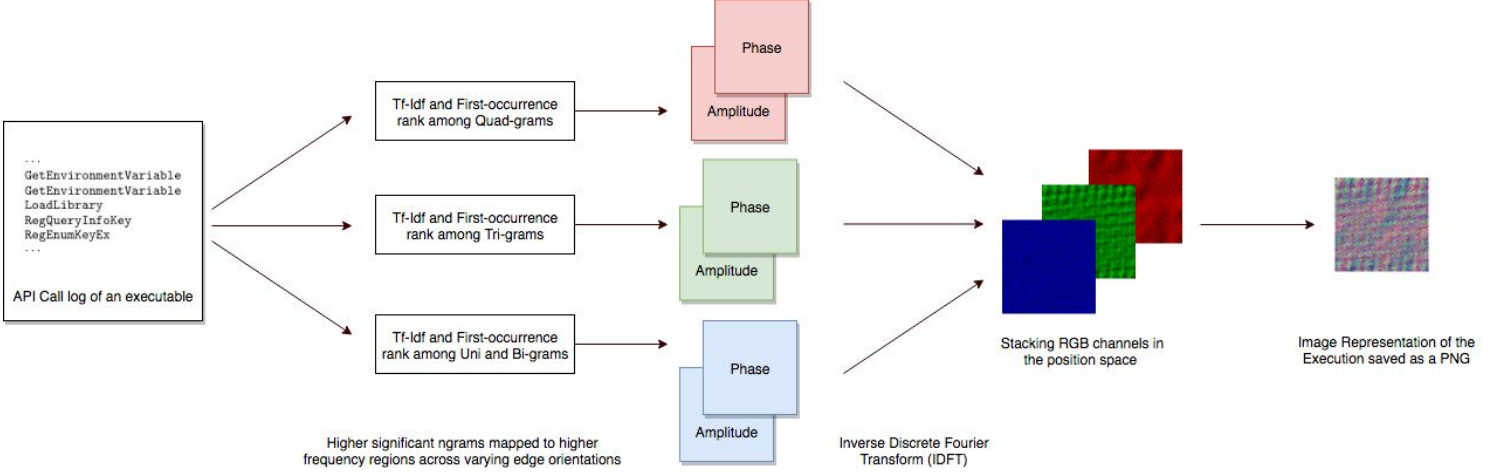


Figure 2: An overview of the image encoding scheme

for the 2-grams, the terms QQ, QB, BP would carry the ranks 1, 2, 3, respectively, by our method. The final ranks are then determined to be 1, 2, 3, 4, 5, 6 for the terms in the order Q, QQ, B, QB, P, BP, respectively. The ranks rescaled to degrees correspond to $60^\circ, 120^\circ, 180^\circ, 240^\circ, 300^\circ, 360^\circ$ phases, respectively, with a default value of 0° for terms that do not appear in the execution. Similarly, the phases computed for the Green channel would be 180° and 360° corresponding to the 3-grams QQB and QBP, respectively, by the same procedure.

8. Given the assigned phases and the amplitudes for an executable i , the position space image for the channel j is computed as

$$\text{Image}_i^j = \text{ContrastNormalize}(\text{IDFT}\{\mathcal{A}_i^j, \mathcal{P}_i^j\}),$$

where $\text{ContrastNormalize}(\cdot)$ linearly rescales the pixel value range per channel after IDFT to $[0, 255]$, that fixes the amplitude of the DC component in the frequency space. Finally, the RGB color image representation of the executable i is obtained by stacking the IDFTs along the depth as

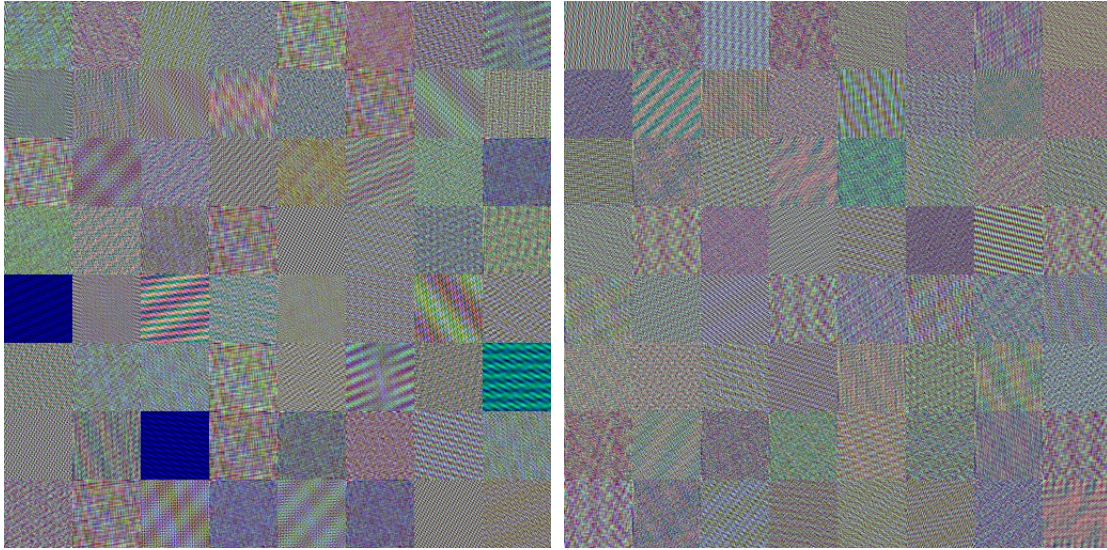
$$\text{Image}_i = [\text{Image}_i^R, \text{Image}_i^G, \text{Image}_i^B].$$

This is stored as a PNG to avoid any loss due to image compressions inherent to alternative file formats such as the JPEG. Figure 2 provides an illustration of the image encoding scheme described above.

Figure 3 shows 64 samples of 64×64 color images generated across the clean and malicious set of files with the steps described above. Each image visually encodes a total of $(4096 - 1) \times 3 = 12,285$ relative tf-idf coefficients of the ngrams across channels, with the first-invocation order captured in the phase of the image. The position space image representation corresponds to a weighted (by tf-idf coefficients) sum of 2D sinusoidal waves at different frequencies, orientations (corresponding to different ngrams), and phases (corresponding to the first-occurrence order). In addition to this, the color channels (Blue, Green, or Red) of the image, representing the ngram type, i.e., $n = 1$ or $2, 3$, and 4 , combine across the depth, giving rise to a spectrum of composite colors for a rich image visualization of the file behavior.

2.3 Decoding Images back to Sequence

Since the Fourier Transform is reversible, one can decode back the information encoded into the images losslessly. The phase of the image at a position in the frequency space can be used to rank the corresponding ngram word to determine its relative order in the output ngram sequence, and the amplitude can be used to derive the relative tf-idf value. The IDF coefficients computed for each ngram word previously, during image generation, can be used to extract the relative (sub-linear) term-frequencies of the ngrams from their relative tf-idfs (amplitudes). This is summarized in the



(a) Non-malicious (clean) files

(b) Malicious files

Figure 3: Samples of 64×64 image representation corresponding to 64 distinct files per category randomly chosen from the dataset. The R, G, B channels represent the 4-gram, 3-gram, and 1,2-grams respectively of the API call words. The amplitude per pixel after DFT is determined by the corresponding tf-idf, and the phase by its relative first-occurrence rank among its channel of ngrams. (Images shown are scaled.)

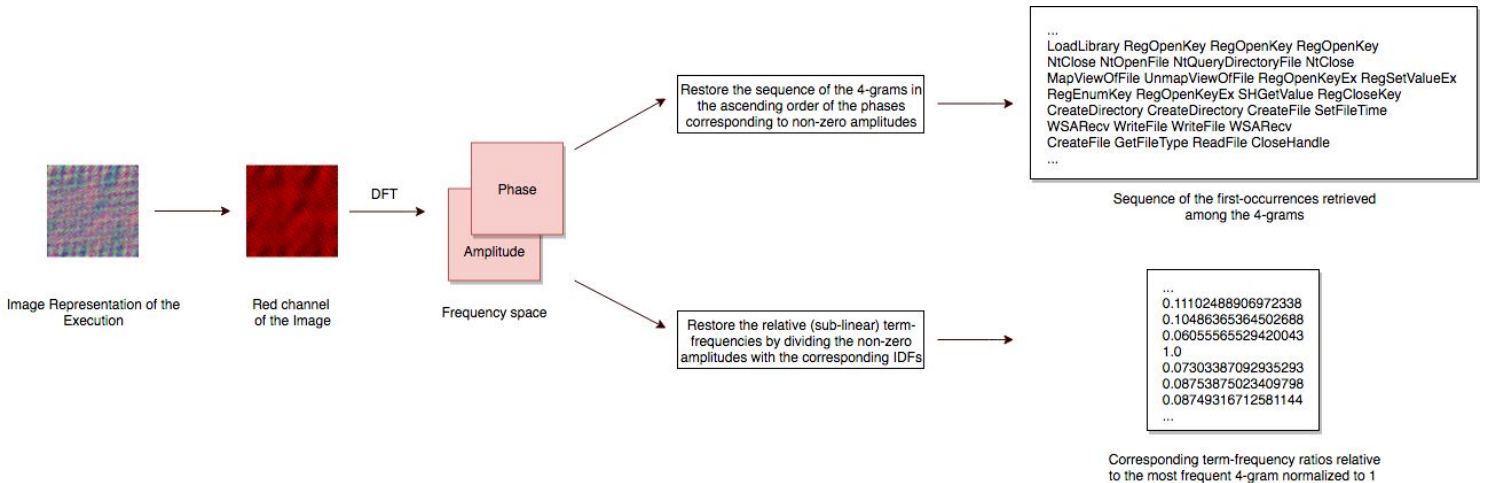


Figure 4: An overview of the image decoding scheme per channel

Figure 4 for the R channel that corresponds to the 4-grams here. The same procedure may be repeated for the other channels to decode the tri- and bi/uni- grams respectively. Being able to decode the images allows interpretability of the decisions made by machine learning classifiers built over the image representations, helping manual analysis of critical false-positives or false-negatives.

3 Applications on Software/Malware Categorization and Smart-Definitions

The described image representation of a file behavior, summarizes the API content and the sequence information into the visible artifacts, such as edges at different orientations, their relative intensities, and the color of the pixels. This enables easy software and malware categorization, manually, by recognizing the similarities and the differences among the executables, based on the visual patterns.

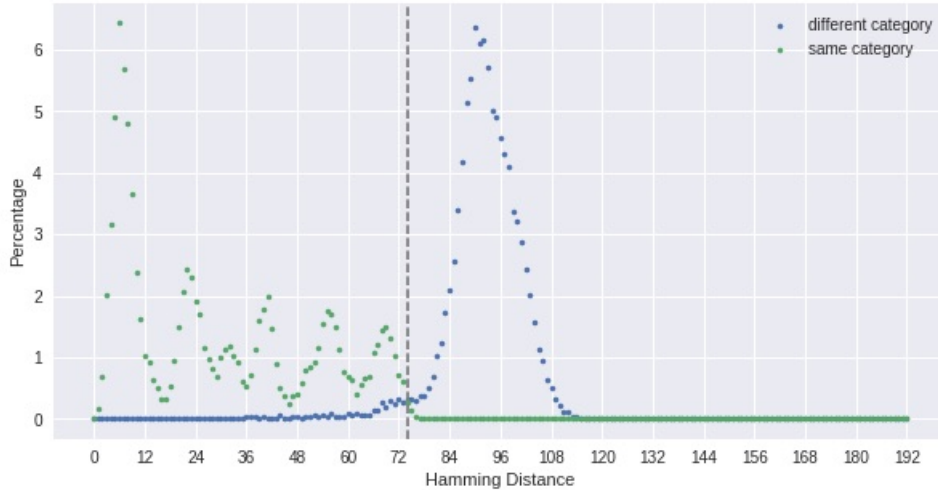


Figure 5: Normalized histogram (bin width = 1) of pair-wise Hamming distances based on a 192-bit perceptual hash, obtained by concatenating the 64-bit dHashes [16] computed per channel, across 254 samples belonging to 21 file categories determined from Symantec’s internal metadata combined with VirusTotal based on file paths, virus names, etc., in-field across clients.

Quick manual malware analysis is critical, especially, for zero-day outbreaks, such as the recent WannaCry attack, to reduce the damaging impact. For such cases, the image representation described, may accelerate the analysis through easy visual comparison with other known malwares. Attribution to related malwares, for instance, can help in faster remediation. It also offers the flexibility of using color filters (Red/Green/Blue) for comparing patterns channel-wise, or even applying band-pass filter operations instead, to only compare the patterns formed by a particular set of ngrams across the given samples.

Categorization may also be easily automated using general image similarity methods and clustering techniques. Since the images have highly ordered structure, unlike the pictures of objects or a scene in real-life, simple distance metrics, such as the pixel-wise Euclidean distance, may be employed for clustering the files into categories. Other methods that summarize the perceptual information or the semantic content of the image (for instance, based on the pre-final layers of a trained deep convolutional neural network) may also be used for image similarity and clustering.

Perceptual hashing techniques (such as the dHash [16], and pHash [17]) applied over the image representation, have an advantage in generalizing well across variants of files with similar behavior, in contrast to the cryptographic hashes (like the SHA256) that are more commonly used for fingerprinting files as anti-malware definitions. Cryptographic hashes change drastically with slight modification in the content, and therefore, carry no meaningful distance metric for measuring similarity. Storing the perceptual hashes of the image representations as *smart-definitions* instead of the SHA256-based hashes, for instance, can improve performance, generalization, and also reduce disk footprint of the antivirus softwares.

Table 3 demonstrates the categorization of softwares/malwares based on the visual similarity of our proposed image representations, while comparing a distance metric based on the dHash [16]. Note that each of the files and the images displayed are different (i.e., have unique SHA256 digests) although some images or the file names, may look similar.

The generalization capability of dHash, for instance, which is based on the pixel gradients, can be evidently noted from the Figure 5. This clearly shows a separation of the pair-wise Hamming distances among the files of the same vs different categories with the grey line representing our proposed cutoff of 74. Stronger cutoffs on the Hamming distance may be required for FP-sensitive applications such as malware classification using the perceptual hash-based similarity.

Table 3: Software categorization based on the images. Note that the images and the files tabulated below are all distinct with different SHA256 digests. The Hamming distances are computed with respect to the first row of each category based on a 192-bit perceptual hash obtained by concatenating the 64-bit dHashes [16] computed per channel. Last three categories demonstrate malware categorization.

Category	Image (scaled)	Filename	Difference Hash or dHash (192-bit Hex)	Hamming Distance
Adobe Acrobat Reader		acrord32-911.exe	631846328c6399ce2a524242229181d5ab5ad52a54ad6a55	0
		acrord32-950.exe	e1810e38e0c31f4c2a42004042a081d5ab5ad52a56ad6a55	31
		acrord32-992.exe	33c1263ee0230fcc0a1e704006bcf9c1cb4a6d2d34b592d2	64
		acrord32-918.exe	33c13e3ee0030fec0a3e784106bdf1c1cb4a6d2d34b59252	68
MySQL Database		mysqladmin.exe (5.1 MB)	00010000000000810f0783c1e0f87c3ead2dad2ab2525559	0
		mysql_embedded.exe (24.1 MB)	81800040000000810f0783c1e0f87c3ead2dad2ab2525559	28
		mysqld.exe (37.9 MB)	00000000000000800f07c3e1f0783c1eadad2ca21252d355	15
TeX Typesetting System		miktex-luatex.exe	a56c4a8b9b92a3ade952f5ac54b13ad42db6464452592cb8	0
		miktex-xetex.exe	a56c4a8b9b92a3ad697371ac4eb13a942da646445269acb8	13
		bg5pdflatex.exe	256c4a8b8b92a9ade95371ac4eb5329429a64644524368b8	20
		miktex-bibtex.exe	256c4a8b8b92a92de95371ac46b13a942da64644526328b8	17
Norton Download Managers		norton_download_manager-1.exe	31899d0a24d883cc8c3698d95a1965349130056d56960de8	0
		nortonn360downloader.exe	31899d4a24d883cc4c3698895a196519b130356dd2d04d6c	20

Continued on next page.

Bluestacks Android Emulator		Bluestacks.exe	282c2b0aaa1a22b223c3d80d652598908655c4526a782ca9	0
		BlueStacksTV.exe	282c2b09aa1b20a323c3c80d65659c910655d452e878aca9	15
Installers		installer_solmysterystolenpower_es.exe	0280009100000088a545cd99b92a6964926d920db28512ac	0
		installer_governorofpokerdeluxe_de.exe	0080009000000088a545cd99b92a6964926d920db285122c	3
Google Updater		googleupdate.exe	52b2f64589919313022000000408174d4a9d52a54a8552d	0
		googleupdate.exe	52b2f62589931313328000800040104254a9d52a54a855af	19
Windows Updates		WindowsServer2003-KB958655.exe	2c2c2622d2d2d999932a4cb64b53a4690603d13578ba2c8f	0
		WindowsInstaller-KB893803-v2-x86.exe	2d2c2612d0d1d909932a4cb26b53a4680627c11178fa3c0f	19
Adware.Graftor		lollipop_12062228.exe	000000000000004880000000040925200000181011124	0
		lollipop_12140006.exe	000000000000004880000000040925a04020981050224	8
Backdoor:Win32/Cycbot.G		asedsle7	009209910241a0082a810080008100c21a54e0021eb4e183	0
		C29.exe	842049a440008249aa01000100810051863cf0020f3cf1c1	42
		DPYRAMYMEG-447.pms.exe.SVD	01042182244992012a810001018100d11a54a10a1ed5a183	32
Babylon PUA/Adware		MyBabylonTB.exe	00000000000000a8810081008100d5aa0000000809085	0
		Babylon.exe	00000000000000a1008100810081528a0000000800085	21

Table 4: 5-Fold cross-validation metrics, and confusion matrices across different FPRs over the OOF predictions of the trained model.

CV Fold	Validation		Training							
	AUC	Logloss	AUC	Logloss	TN	FN	TP	FP	TPR%	FPR%
fold1	0.9712	0.3038	0.99	0.0036	1411	1125	1137	1	50.27	0.0708
fold2	0.9754	0.2889	0.99	0.0038	1405	687	1575	7	69.63	0.496
fold3	0.9716	0.3205	0.99	0.0042						
fold4	0.9743	0.3036	0.99	0.0040						
fold5	0.9720	0.2948	0.99	0.0050						
all OOFs	0.9727	0.3023								

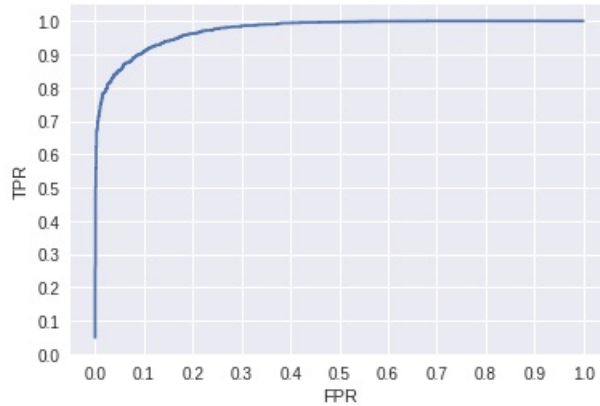


Figure 6: ROC curve over the OOF predictions of the trained XGBoost model.

Recent works on data-driven perceptual hashing algorithms involving deep convolutional siamese networks with binary output neurons [18–22], that are tailored to the domain of application, promise further generalization of the hash fingerprints at lower FP rates.

4 Simple Malware Classifier trained on the image pixels

In this section we validate our proposed scheme of mapping the file behavior to the RGB image space by investigating the efficacy of a simple boosted-tree based model (using the XGBoost package [11]) for malware classification. The model is trained directly over the flattened raw pixels of the image representation corresponding to the 1,412 clean and 2,262 malicious samples. The model is trained to minimize the logloss cost function. The hyperparameters [†] were chosen over a randomized grid search evaluated by the out-of-fold (OOF) validation AUC score.

The OOF cross-validation scores, ROC curve, and the confusion matrices at different FPRs (where ‘positive’ refers to a conviction and ‘negative’ to an exoneration) of the trained model are summarized in the Table 4 and Figure 6. The model achieves a TPR of about 50% at a low FP rate of 0.071% (corresponding to a single FP). The results show that the raw pixels of our image representation encode significant information across the API call sequence to discriminate between the two classes (malicious or benign) efficiently.

5 Modeling Malware Behaviors with Generative Adversarial Networks

Generative Adversarial Networks or GANs, first invented by Goodfellow *et al.* [10] in 2014, are a class of generative models that approximate the inherent distribution of the input data, based on a finite sample represented by the training dataset, using backpropagation over a minimax objective

[†]https://xgboost.readthedocs.io/en/latest/python/python_api.html

function involving two competing sub-networks — the discriminator and the generator — playing an adversarial zero-sum game, in an unsupervised setting, iteratively, where the generator minimizes the predictability of the discriminator in classifying the real from the *synthetic* data that is generated by the generator, and, in turn, the discriminator competes by learning on the differences.

The weights of the discriminator network are updated to minimize the loss in the classification of the fake (generated) from the real samples, whereas, the generator is updated, backpropagating the discriminator’s error signal, to maximize the classification loss of the discriminator, by generating fake samples which look more real. Soon the generator is able to sample images highly resembling the input data while the discriminator saturates to being highly uncertain in classifying them from the real ones. The trained generator G , capturing the true input distribution, can then be sampled to interpolate or extrapolate the training data.

GANs, as originally proposed by Goodfellow *et al.*, were limited by major challenges such as training instability, high sensitivity to network hyperparameters, difficulty in choosing the right learning rates for the discriminator and the generator (so that neither saturates too fast), in addition to not being inherently convolutional for modeling image datasets. In 2015, Radford *et al.* [23] introduced a deep and convolutional version of the GANs called DC-GANs with improved training stability for modeling the image datasets, generating realistic synthetic images, with interesting vector arithmetic in the input noise space that samples the learnt distribution of the generator. However, it still suffered from problems such as uninterpretable loss function that didn’t always correlate with the quality of the generated images, sensitivity to network architecture and hyperparameters, etc.

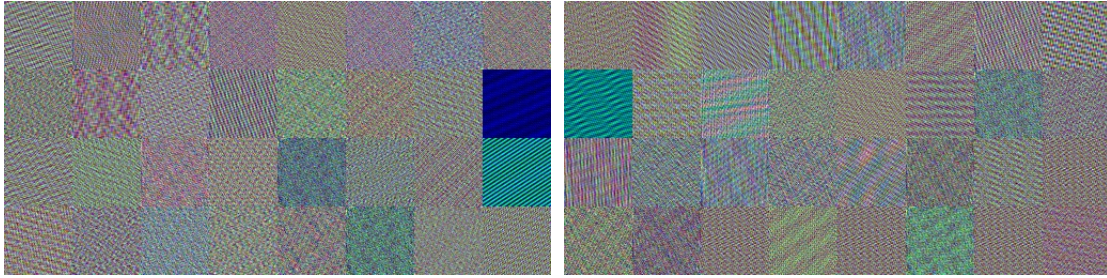
In 2017, Arjovsky *et al.* [24] proposed an alternative cost function for the GAN that estimates the Wasserstein distance of the synthetic to the real data distribution under the constraint of weight clipping, with the discriminator (or the “critic”) predicting a value function instead of the class labels. They showed that, unlike the previous works, the loss function correlated well with the output quality of the generated images, in addition to an improved stability of the training. However, using weight-clipping strongly regularized the model with a high sensitivity to the clipping parameter c , limiting its capacity in capturing the higher moments of the data distribution, as shown by Gulrajani *et al.* in [13] who suggested penalizing the gradient norm instead of clipping the weights. Their model, referred to as WGAN-GP, drastically improved the training stability across a wide variety of network architectures, notably also involving also the residual connections [1], with minimal or no tuning of the GAN hyperparameters. In addition, the modified cost function of the GAN also ensured that the generator continued improving significantly even after the discriminator neared saturation.

5.1 Training

We trained a WGAN-GP model over the image representation of the malicious file behaviors that inherently captures the API content along with the sequence of the first-occurrence. Once the generator is trained to model the distribution of the malicious behavior, one can sample instances that represent new malware, thereby, emulating a malware author against which a malware classifier may be tuned, tested, or trained for proactive protection.

Our dataset consisted of $64 \times 64 \times 3$ image representations of 2,262 distinct malicious samples (excluding the 250 malicious samples out of the 500 used for mapping the top significant ngrams to the image frequencies). We divided the set into a 80:20 train:test holdout split to train the WGAN-GP model on 1,809 and validate on 453 image representations of distinct malicious samples. A sample of the training and the validation images used are shown in the Figure 7. The architecture of the generator and the critic network of the trained WGAN-GP model is summarized in the Figure 8, that has been one of the many architectures validated by Gulrajani *et al.* in [13] who demonstrated competitive results of sample generation quality on the $128 \times 128 \times 3$ LSUN bedrooms dataset [25].

The critic:generator training iteration ratio is kept at 5 : 1, i.e., for every 5 training iterations of the critic, the generator is updated once. A default value of $\lambda = 10$, as suggested in [13], is used as the gradient penalty hyperparameter in the WGAN-GP loss function. A batchsize of 64 is used for computing the gradient update per iteration that is parallelized into batches of 16 training samples (data parallelisation) across 4 nVIDIA GTX TITAN X GPUs with 12 GB of available memory and 3,072 CUDA cores each. Adam [26] optimization algorithm was used for training the network with a learning rate of 0.0001, $\beta_1 = 0$, and $\beta_2 = 0.9$. The synthetic images are sampled from the trained



(a) Sample of the images used for training.

(b) Sample of the images used for validation.

Figure 7: Sample of the image representations of malicious files used for training the WGAN-GP model.

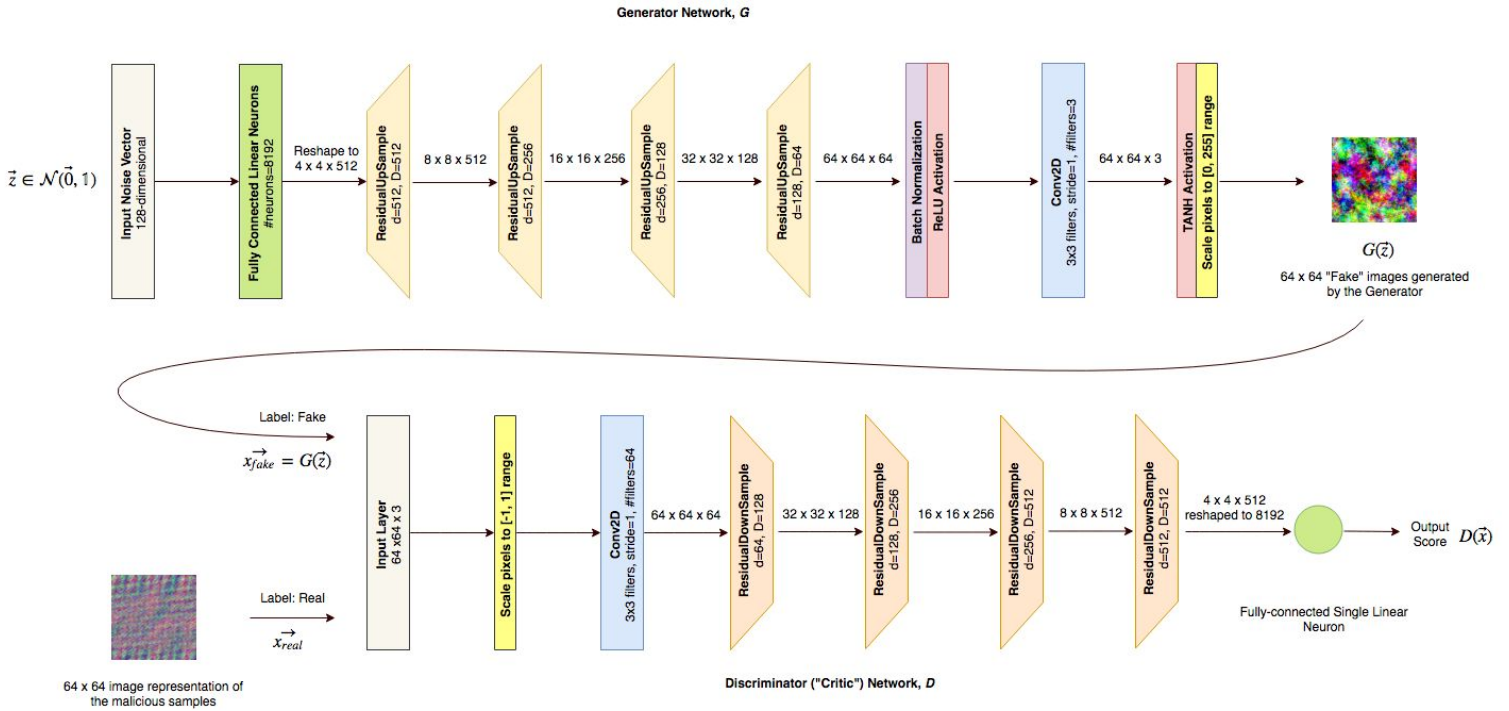


Figure 8: Architecture of the generator and the critic networks of the WGAN-GP model trained where the *ResidualUpSample* and the *ResidualDownSample* blocks are as defined in the Figures 9a and 9b, respectively.

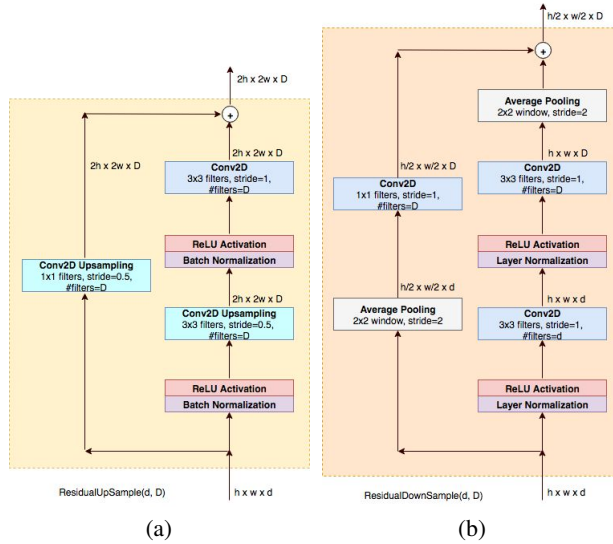


Figure 9: Architecture of the residual blocks used in the (a) generator, and the (b) critic networks, respectively.

generator with 128-dimensional noise vector inputs (\vec{z}) that are, in turn, sampled from a Gaussian standard normal distribution with zero mean and unit variance ($\mathcal{N}(\vec{0}, \mathbf{1})$)[†].

The model trained for about a day across 45,000 generator iterations with final negative critic losses (averaged across mini-batches of an epoch) of 0.4262 on the training set, and 1.08365 on the validation set. Figure 10a describes the training cost (across each iteration) and the validation cost (for every 10 iterations) of the critic on a minibatch of 64. This shows a stable training run without any overfitting. The Wasserstein distance estimate converges close to zero consistently across the training and the validation. Figure 10b shows a sample of 64 synthetic images generated by the trained generator network G .

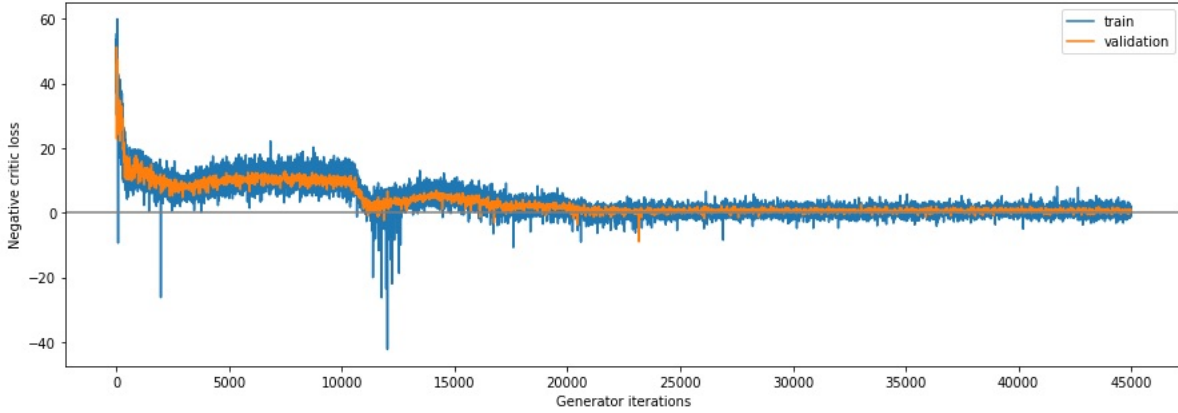
5.2 Applications

Proactive Protection against Zero-Day Malwares. The synthetic images sampled from the learned distribution, interpolating or extrapolating the known dataset, are representative of new malware behaviors *authored* by the generator. Such generated samples may be augmented with the original training datasets and can be used for modeling behavior-based malware classifiers, for protection against zero-day malicious behaviors that are captured by the trained generator’s distribution. Malware classifiers that can take such advantage of the synthetic images, needn’t necessarily be based only on the image representation. As the images may be decoded back to the ngram sequence and the corresponding term-frequencies that it visually represents, the synthetic images generated, therefore, can further be used by other behavioral event-based rules, signatures and ML applications.

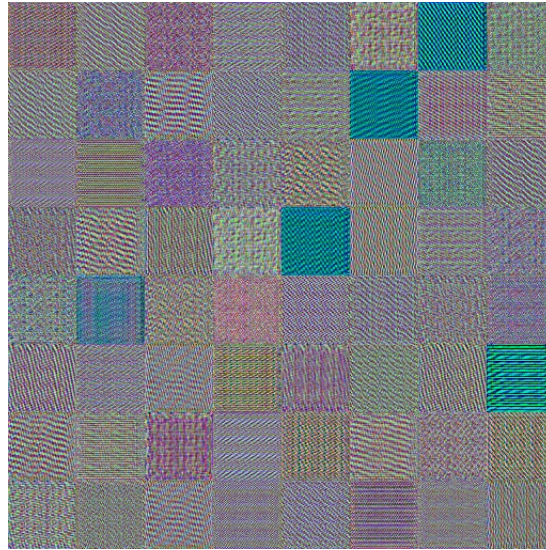
Interpreting the Synthetic Samples. The synthetic images sampled from the learned distribution may be interpreted for further analysis by decoding them back to the corresponding ngram sequence and the relative term-frequencies, as demonstrated in the Figure 11. Ability to have such a decomposition offers the advantage of analyzing malicious behaviors that have not yet been observed in-field but are a part of the current threat distribution or *trend* captured by the generator. These decoded sequences may further be used to define behavior-based string-signatures, or augment the training sets of general behavior-based malware classifiers, as discussed above.

Testing and Tuning Malware Classifiers. Behavior-based malware classifiers may be tuned or tested against the trained generator that takes the role of a malware emulator in synthesizing new

[†]Network architecture and the hyperparameters of the model were chosen out of those evaluated by Gulrajani *et al.* on the LSUN bedrooms dataset in [13].



(a) The negative critic loss of the model converging towards a minimum as the network trains. The images used for validation are from a different set of executables not included in the training set.



(b) Generated sample of synthetic images from the trained generator after 45,000 generator iterations. (Images shown are scaled.)

Figure 10: Training metrics, and sample generated images of the WGAN-GP model trained on the malicious image dataset.

malicious behavior, similar to the advantage that the malware authors have been having in being able to test their malicious payload against security softwares at their disposal.

Generating Malware Hybrids with Vector Arithmetic. Radford *et al.* [23] first showed that the input space of the noise vectors modeled the semantic information of the final generated images in subtle ways that enabled the manipulation of the visual artifacts of the generated image with simple vector arithmetic of the inputs. Specifically, they showed, that manipulating the input noise vectors corresponding to the output images of *men with glasses*, by intuitive vector arithmetic, gave resultant vectors that sampled images consisting of *women with glasses*, when fed through the generator G trained on a dataset of human faces. They showed that the image output of $G(\vec{z}_{\text{man,glasses}} - \vec{z}_{\text{man,no glasses}} + \vec{z}_{\text{woman,no glasses}})$ resembled that of a *woman with glasses*. But, a similar arithmetic in the pixel-space, given by $G(\vec{z}_{\text{man,glasses}}) - G(\vec{z}_{\text{man,no glasses}}) + G(\vec{z}_{\text{woman,no glasses}})$, produced blurry images with all the semantic features of a face washed out. This suggests that the input noise space models the structure of the underlying data in a way, that when combined under an arithmetic operation, samples an image with a combination of specific semantic artifacts (such as the smile, complexion, wearing

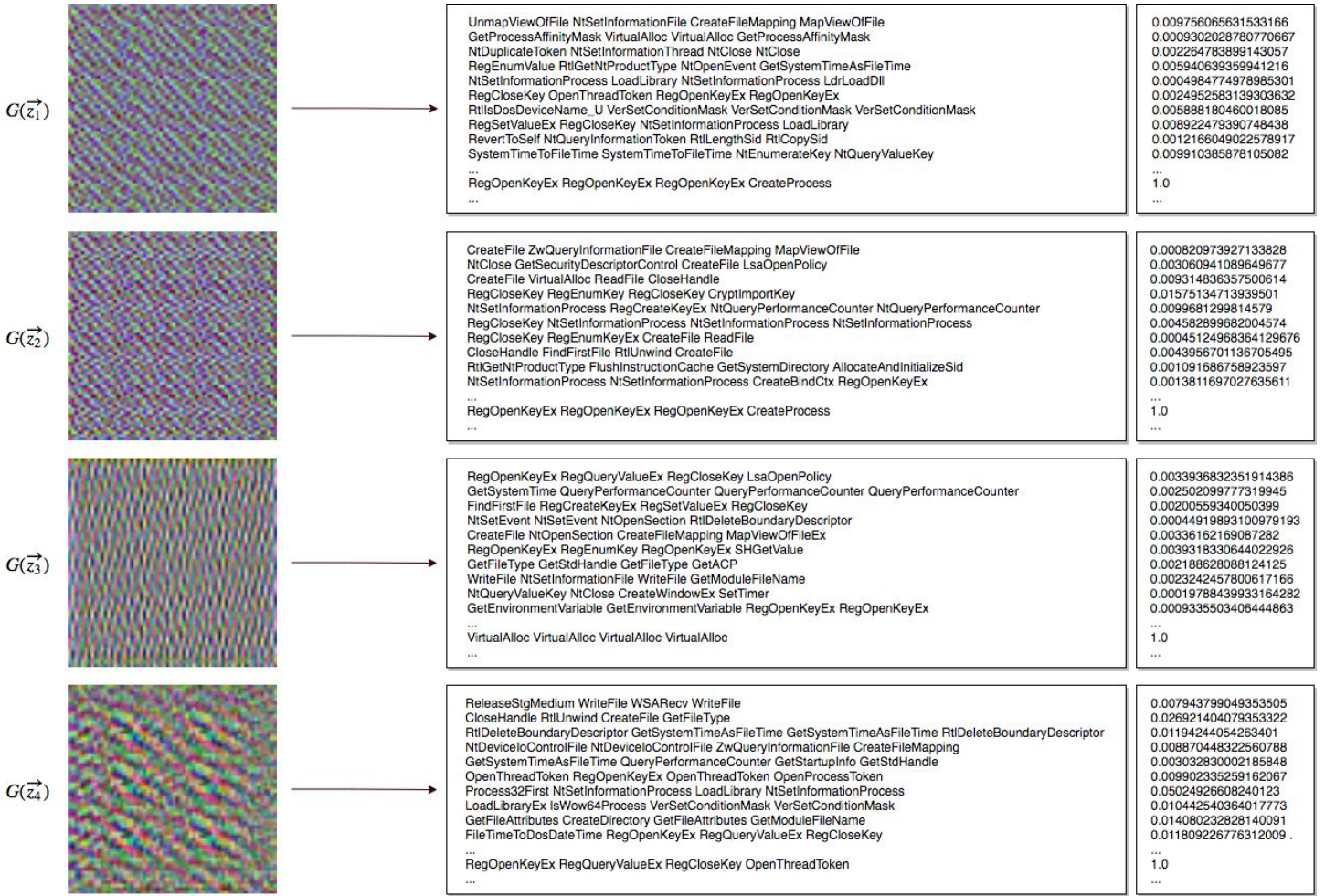


Figure 11: Interpreting the synthetic malware by decoding the generated image representation into a sequence of the first-occurrence of the ngram words along with their corresponding relative (sub-linear) term-frequencies with respect to the highest frequent ngram per channel whose tf is normalized to 1. For the demonstration above, $n = 4$ (Red channel) is chosen. A similar decomposition may be obtained for 1,2-grams or 3-grams corresponding to the Blue or the Green channels, respectively, as discussed in Section 2.3. (Images shown are scaled.)

spectacles etc) while preserving the overall high-level semantics. That is, the resultant generated images from input vectors created through such arithmetic operations, still *looked* like a face.

This further suggests that such arithmetic in the noise vector space of malware image representations, may be exploited to combine behavioral features across malwares, such as, for instance, the event of adding an entry to the registry, frequent disk I/O calls infecting good files, using power shell to connect remotely, etc., such that the resultant represents a hybrid malware that is coherently combined to still retain the *malicious* semantics. Figure 12 demonstrates an example of a simple arithmetic of combining four malwares (those in Figure 11) in the input noise vector space and the pixel space, highlighting the differences in terms of the decoded sequences of 4-grams with the corresponding relative term-frequencies.

6 Conclusions and Future Work

In this work, we demonstrated a novel way of representing dynamic file behavior of an executable in the image-space for effective visualization, and with applications of easy manual/automatic software and malware categorization. The raw pixels of the image representation were shown to

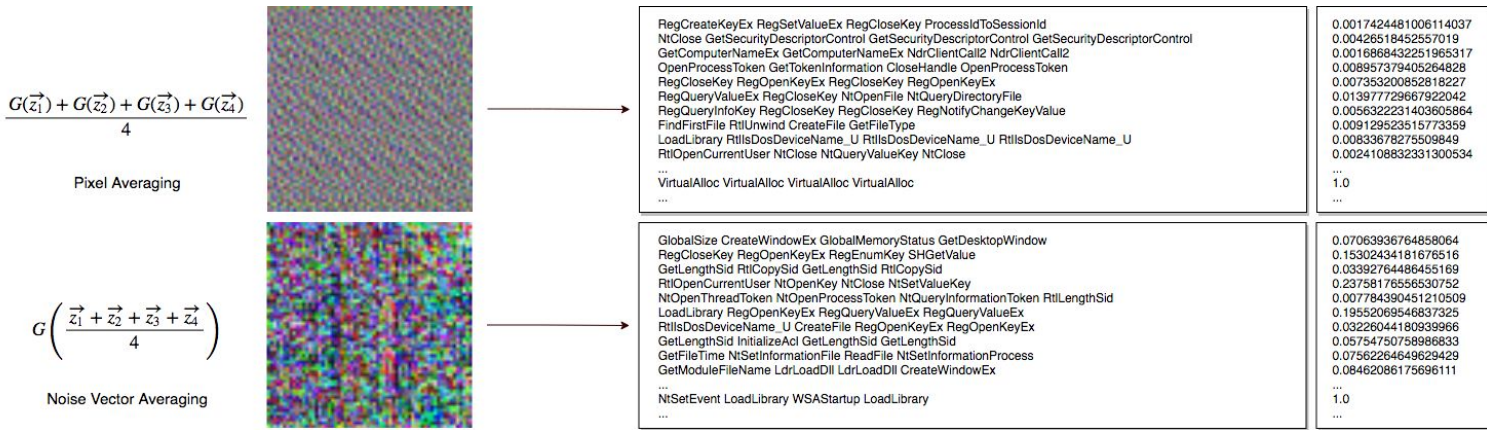


Figure 12: Comparing the averages of the malware images in the pixel-domain and the input noise vector space. We propose a novel method of generating hybrid malwares from a set of generated malwares based on noise vector arithmetic on visual concepts, first demonstrated by Radford *et al.* [23] on a dataset of human faces. (Images shown are scaled.)

encode significant information to efficiently classify malwares from clean files using boosted-trees. Additionally, the image representation was shown to be compatible across deep learning architectures (generative or discriminative) involving the convolution filter maps. Finally, we described the applications of GANs in modeling the distribution of malicious behaviors, and in creating new and hybrid malware image representations, that could be decoded to the individual API call information and the first-invocation sequence, for proactive protection.

Future works may include research on incorporating the arguments and the DLL information of the API calls into the images, comparing the results presented in this paper, for possible efficacy improvements. Another possible research direction includes modeling the malware behaviors directly over the API call sequences using Sequence GANs [27]. Sequence GANs are currently at a nascent state in terms of training stability and sequence generation quality. One may also experiment with the other families of GANs such as the conditional GANs [28] that exploit the class labels (malicious or clean) in modeling the class-conditional distributions of the input data.

Also, the vector arithmetic heuristic proposed over the image representations of the malware behaviors, for combining malwares, is only easy to formulate, given the vector components capture different recognizable unique strains of the input distribution. That is, each component models a unique semantic aspect of the malicious behavior. The InfoGAN [29] architecture helps to achieve the above by creating a disentangled representation of the semantic aspects, using an augmented set of inputs (called latent code) which, unlike the WGAN-GP model, can be used to deterministically tweak the resultant malware hybrid.

We hope our work inspires further research into bridging the gap in security with the state-of-the-art deep learning technologies for an end-to-end intelligent proactive protection against unseen and unknown threats.

References

- [1] K. He, X. Zhang, S. Ren and J. Sun. Deep residual learning for image recognition. *IEEE Conference on Computer Vision and Pattern Recognition (CVPR)*, 770–778, 2016.
- [2] K. Fukushima. Neocognitron: A self-organizing neural network model for a mechanism of pattern recognition unaffected by shift in position. *Biological Cybernetics* 36 (4), 93-202, 1980.
- [3] Y. LeCun, P. Haffner, L. Bottou, and Y. Bengio. Object recognition with gradient-based learning. *Shape, Contour and Grouping in Computer Vision*, Springer, 319–345, 1999.
- [4] A. Krizhevsky, I. Sutskever, and G.E. Hinton. ImageNet classification with deep convolutional neural networks. *Advances in Neural Information Processing Systems (NIPS)* 25, 1097–1105, 2012.

- [5] M. Jaderberg, K. Simonyan, A. Zisserman, and K. Kavukcuoglu. Spatial transformer networks. *Advances in Neural Information Processing Systems (NIPS)* 28, 2017–2025, 2015.
- [6] S. Sabour, N. Frosst, and G.E. Hinton. Dynamic routing between capsules. *Advances in Neural Information Processing Systems (NIPS)* 30, 3856–3866, 2017.
- [7] D. Duvenaud, D. Maclaurin, J. Iparraguirre, R. Bombarell, T. Hirzel, A. Aspuru-Guzik, and R.P. Adams. Convolutional networks on graphs for learning molecular fingerprints. *Advances in Neural Information Processing Systems (NIPS)* 28, 2224–2232, 2015.
- [8] E. Raff, J. Barker, J. Sylvester, R. Brandon, B. Catanzaro, and C. Nicholas. Malware detection by eating a whole EXE. *arXiv preprint arXiv:1710.09435*, 2017.
- [9] M. Allamanis, M. Brockschmidt, and M. Khademi. Learning to represent programs with graphs. *International Conference on Learning Representations (ICLR)*, 2018.
- [10] I. Goodfellow, J. Pouget-Abadie, M. Mirza, B. Xu, D. Warde-Farley, S. Ozair, A. Courville, and Y. Bengio. Generative adversarial nets. *Advances in Neural Information Processing Systems (NIPS)* 27, 2672–2680, 2014.
- [11] T. Chen, and C. Guestrin. XGBoost: A scalable tree boosting system. *Proceedings of the 22nd ACM SIGKDD International Conference on Knowledge Discovery and Data Mining*, 785–794, 2016.
- [12] W. Hu, and Y. Tan. Generating adversarial malware examples for black-box attacks based on GAN. *arXiv preprint arXiv:1702.05983*, 2017.
- [13] I. Gulrajani, F. Ahmed, M. Arjovsky, V. Dumoulin, and A. Courville. Improved training of Wasserstein GANs. *Advances in Neural Information Processing Systems (NIPS)* 30, 5767–5777, 2017.
- [14] F. Pedregosa *et al.* Scikit-learn: Machine Learning in Python. *Journal of Machine Learning Research (JMLR)* 12, 2825–2830, 2011.
- [15] C.D. Manning, P. Raghavan, and H. Schütze. Introduction to Information Retrieval. Cambridge University Press, 2008.
- [16] N. Krawetz. Blogpost – <http://www.hackerfactor.com/blog/?/archives/529-Kind-of-Like-That.html>. Retrieved July 10, 2018.
- [17] C. Zauner. Implementation and benchmarking of perceptual image hash functions. Master’s thesis, Upper Austria University of Applied Sciences, Hagenberg Campus, 2010.
- [18] M.M. Emara, M.W. Fahr, and M.B. Abdelhalim. A neural network approach for binary hashing in image retrieval. *Proceedings of the International Conference on Advanced Intelligent Systems and Informatics*, Springer, 395–406, 2016.
- [19] A. Jose, S. Yan, and I. Heisterklaus. Binary hashing using siamese neural networks. *IEEE International Conference on Image Processing (ICIP)*, 2916–2920, 2017.
- [20] G. Song, and X. Tan. Hierarchical deep hashing for image retrieval. *Frontiers of Computer Science* 11 (2), Springer, 253–265, 2017.
- [21] H. Liu, R. Wang, S. Shan, and X. Chen. Deep supervised hashing for fast image retrieval. *IEEE Conference on Computer Vision and Pattern Recognition (CVPR)*, 2064–2072, 2016.
- [22] K. Lin, H. Yang, J. Hsiao, and C. Chen. Deep learning of binary hash codes for fast image retrieval. *IEEE Conference on Computer Vision and Pattern Recognition Workshops (CVPRW)*, 27–35, 2015.
- [23] A. Radford, L. Metz, and S. Chintala. Unsupervised representation learning with deep convolutional generative adversarial networks. *arXiv preprint arXiv:1511.06434*, 2015.
- [24] M. Arjovsky, S. Chintala, and L. Bottou. Wasserstein GAN. *arXiv preprint arXiv:1701.07875*, 2017.

- [25] F. Yu, A. Seff, Y. Zhang, S. Song, T. Funkhouser, and J. Xiao. LSUN: Construction of a large-scale image dataset using deep learning with humans in the loop. *arXiv preprint arXiv:1506.03365*, 2015.
- [26] D.P. Kingma, and J. Ba. Adam: A method for stochastic optimization. *International Conference on Learning Representations (ICLR)*, 2015.
- [27] L. Yu, W. Zhang, J. Wang, and Y. Yu. SeqGAN: Sequence generative adversarial nets with policy gradient. *Thirty-First AAAI Conference on Artificial Intelligence*, 2017.
- [28] M. Mirza, and S. Osindero. Conditional generative adversarial nets. *arXiv preprint arXiv:1411.1784*, 2014.
- [29] X. Chen, Y. Duan, R. Houthoofd, J. Schulman, I. Sutskever, and P. Abbeel. InfoGAN: Interpretable representation learning by information maximizing generative adversarial nets. *Advances in Neural Information Processing Systems (NIPS)* 29, 2172–2180, 2016.